Global Biogeochemical Cycles

RESEARCH ARTICLE
10.1029/2018GB005927

The Seasonality of Physically Driven Export at Submesoscales in the Northeast Atlantic Ocean

Zachary K. Erickson[1] and **Andrew F. Thompson**[1]

[1]Division of Geological and Planetary Sciences, California Institute of Technology, Pasadena, CA, USA

Key Points:
- Seaglider measurements captured a full annual cycle of physical and optical data at submesoscale resolution
- Stratification at the base of the mixed layer plays a critical role in controlling export from submesoscale motions
- Temporal offset between peak productivity and submesoscale activity limits physical carbon export in this location

Correspondence to:
Z. K. Erickson,
zerickso@caltech.edu

Citation:
Erickson, Z. K., & Thompson, A. (2018). The seasonality of physically driven export at submesoscales in the northeast Atlantic Ocean. *Global Biochemical Cycles*, *32*, 1144–1162. https://doi.org/10.1029/2018GB005927

Received 13 MAR 2018
Accepted 14 JUN 2018
Accepted article online 22 JUN 2018
Published online 9 AUG 2018
Correction 30 AUG 2018

This article was corrected on 30 AUG 2018. See the end of the full text for details.

Abstract Submesoscale dynamics $\mathcal{O}(1-100$ km) are associated with enhanced vertical velocities and evolve on a time scale similar to that of biological production (hours to days). Here we consider an annual cycle of submesoscale dynamics and their relation to productivity and export in a small (20×20 km) region of the northeast Atlantic Ocean. In this region, a springtime bloom is initiated by restratification of the mixed layer in June, although intermittent shoaling of the mixed layer maintains phytoplankton populations throughout the year. An optical community index suggests a dominance of large species (e.g., diatoms) during spring and picophytoplankton during the winter. We review three types of submesoscale instabilities—mixed layer (baroclinic), gravitational, and symmetric—and consider the impact of each on export of fixed carbon out of the surface layer. Mixed layer instabilities can potentially export material out of the mixed layer during winter, although the vertical velocity across the base of the mixed layer is sensitive to the parameterization scheme. Symmetric instabilities, in contrast, provide a clear mechanism for rapid export out of the mixed layer. A crucial factor determining export potential is the strength of the pycnocline at the base of the mixed layer. Export production is sensitive to the degree of overlap that exists between intense submesoscale activity associated with deep mixed layers in the winter and high productivity associated with the spring restratification, meaning that physically driven export of fixed carbon will likely happen over a short time window during spring.

1. Introduction

Marine biota account for approximately half of global primary productivity (Field et al., 1998), yet the residence time of carbon in the biosphere is an order of magnitude smaller in the ocean than on land. There is a clear seasonal cycle of phytoplankton biomass, with bloom dynamics in the middle to high latitudes dominating during spring. Blooms develop on time scales of days, which is much shorter than the evolution time scale of weeks for mesoscale eddies and fronts (where *mesoscale* signifies length scales L such that the Rossby number $Ro = \frac{U}{fL} \ll 1$, where f is the planetary vorticity and U is a characteristic velocity). Biological processes are therefore often implicitly assumed to happen in a stationary physical regime. However, research in the field of submesoscale dynamics (motions characterized by $Ro \sim 1$) has shown the importance of scales of $\mathcal{O}(1-100$ km) in stimulating large vertical velocities and lateral and vertical tracer transport (Brannigan, 2016; Lévy et al., 2012; Mahadevan & Tandon, 2006; McWilliams, 2016; Rosso et al., 2014). Submesoscale dynamics evolve on a time scale of hours to days, which is similar to the time scale of biological production. The ability of submesoscale dynamics to influence biological production and export fixed carbon out of the surface ocean is not well understood.

Phytoplankton blooms are typically considered to be a result of restratification-driven shoaling of the mixed layer into the euphotic zone (Mahadevan et al., 2012; Sverdrup, 1953). Blooms are generally dominated by diatoms, which exist at low concentrations during the winter (Kostadinov et al., 2009) and may be maintained during this time through small-scale restratification events (Lacour et al., 2017). However, phytoplankton biomass in the surface ocean does not necessarily lead to carbon export. Much progress has been made considering this problem in a one-dimensional Lagrangian framework, where the important processes controlling export are aggregation, sinking, and predation with the associated formation of fecal pellets and other detritus (Ducklow et al., 2001; Stemmann et al., 2004).

Sinking of particulates, whether in the form of single organisms, aggregates, detritus, or fecal pellets, is not the only method by which carbon is exported. Physical subduction of water masses can also induce export. At the largest scales, this is the reason for the observed distribution of chlorofluorocarbons, nutrients, and oxygen in the ocean interior (Broecker et al., 1998). One mechanism for this subduction is due to surface

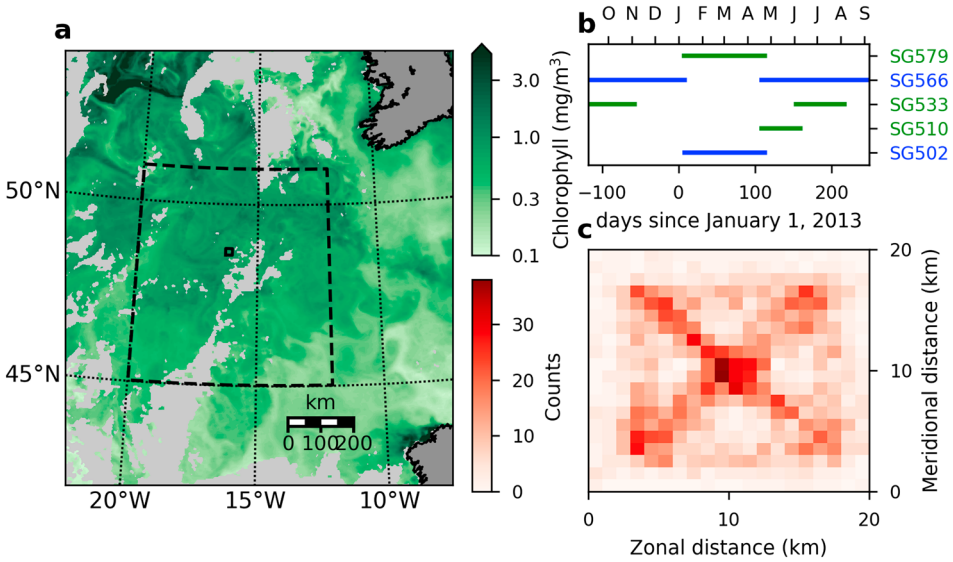

Figure 1. (a) Average surface chlorophyll concentration from 12 to 19 July 2013 from MODIS Aqua. Light gray gives cloud-covered areas, and dark gray are land masses (Ireland in the upper right, and the Iberian peninsula in the lower right). Note the logarithmic color bar. OSMOSIS region is shown in the black box centered at 16.2°W, 48.7°N, and the region used for the satellite-derived bloom time series in Figure 2 is shown by the black dashed line. (b) Deployment periods for each of the five gliders. Blue gliders are hereafter referred to as *Glider 1*; green lines are *Glider 2* (Table 1). (c) Histogram of surface locations for each vertical glider profile over the entire five-glider deployment, encompassing a total of 7,458 profiles. Each grid point is 1 × 1 km. MODIS = Moderate Resolution Imaging Spectroradiometer; OSMOSIS = Ocean Surface Mixing, Ocean Submesoscale Interaction Study.

buoyancy forcing (heating or precipitation) during spring capping the deep wintertime mixed layer, which in some locations leads to export either through net advection of high-biomass waters deeper into the interior along isopycnals or through consumption of dissolved organic carbon and subsequent particulate sinking (Carlson et al., 1994; Sarmiento, 1983). However, processes at the submesoscale, where the effect of planetary rotation is no longer dynamically dominant, can drive vigorous vertical motions of up to hundreds of meters per day (Lévy et al., 2012). The effect of these small-scale vertical motions in bringing nutrients from depth into the euphotic layer and stimulating production is seen in high-resolution models (Brannigan, 2016; Lévy et al., 2001; Mahadevan & Archer, 2000). Observations also suggest that these vertical motions can subduct water high in chlorophyll below the mixed and euphotic layers (Erickson et al., 2016; Hood et al., 1991; Washburn et al., 1991). The combined effects of submesoscale motions may dominate export in much of the highly productive ocean (Omand et al., 2015).

Submesoscale dynamics are particularly active in regimes with large lateral shear, such as boundary currents (Molemaker et al., 2015; Rocha, Gille, et al., 2016; Rocha, Chereskin, et al., 2016; Thomas et al., 2013, 2016) or the Antarctic Circumpolar Current (Erickson et al., 2016). However, a growing body of evidence shows that vigorous submesoscale activity is present even in the relatively quiescent open ocean (Brannigan et al., 2015; Su et al., 2018; Thompson et al., 2016). The open ocean is generally oligotrophic or mesotrophic (commonly defined as surface chlorophyll values below 1 mg/m^3) but constitutes a large fraction of total export due to its large areal extent (Laws et al., 2000). Seasonality in the energy content of submesoscale motions is related to seasonality in the mixed layer depth (MLD; Callies et al., 2015; Sasaki et al., 2014) and may affect export throughout the year.

Although high-resolution models show the importance of submesoscale motions in the injection of nutrients into the mixed layer and subduction of particulate organic carbon (POC) out of the mixed layer (Mahadevan, 2016), few in situ studies have been able to resolve these scales. In the Sargasso Sea, Estapa et al. (2015) used high-resolution O_2/Ar and thorium isotope measurements to show that net community production and export production were uncorrelated at scales less than 10 km. They associated this short decorrelation length scale with small-scale vertical circulation systems (Lévy et al., 2012). Off the coast of California, Stukel et al. (2017) found evidence of carbon export through downward transport along isopycnals in frontal regions and estimated that this subductive flux was comparable in magnitude to that of export through particle sinking.

They hypothesized that similar mechanisms would exist in eastern boundary upwelling systems worldwide, representing a significant flux in the global carbon budget. In another instance, Omand et al. (2015) used Lagrangian measurements of phytoplankton and export in the North Atlantic (Alkire et al., 2012) to estimate the effect of submesoscale dynamics, through baroclinic instability in the mixed layer, on export production. Using satellite and climatological data, they found that eddy-driven subduction from submesoscale instabilities could account for 30–60% of export in much of the productive ocean.

Here we use observations from Seagliders (hereafter, gliders) in the northeast Atlantic Ocean to examine the seasonal cycle of phytoplankton and assess the potential for export due to submesoscale instabilities throughout the year. In contrast to the Lagrangian approach typically used (e.g., Alkire et al., 2012), we do not follow a water mass or characterize the evolution of a single water parcel. Instead, we continuously measure properties in a 20 × 20 km region of the ocean (Figure 1), providing a yearly cycle of biological variables such as fluorescence, backscatter, and oxygen, as well as physically relevant measurements of horizontal and vertical buoyancy gradients at scales of 3–5 km in the horizontal and 2 m in the vertical. These latter measurements allow the calculation of potential vorticity (PV), which we use to characterize instabilities and link them to export production in this region. The unique aspect of this data set is its resolution and duration; we measure biological and physical properties at submesoscale resolution from September 2012 to September 2013 and can therefore study the full seasonal cycle of production and submesoscale dynamics.

We consider the theoretical framework of submesoscale instabilities using buoyancy gradients and PV in section 2, followed by our observations and results in sections 3 and 4. In section 5 we discuss how our observational results are affected by the theoretical mechanisms outlined in section 2 at the event level and their relevance for annual export estimates, before concluding with section 6.

2. Theoretical Framework

At large scales $\mathcal{O}$(100+ km), the ocean is approximately in hydrostatic and geostrophic balance, meaning that the vertical and horizontal pressure gradients are balanced by gravity and the planetary vorticity (Coriolis force), respectively. Vertical velocities are weak, and horizontal flows are nondivergent and evolve over time scales of weeks or longer. At smaller scales $\mathcal{O}$(1–100 km), the effect of planetary rotation is less dominant, and ageostrophic dynamics may become important. Since global ocean models are rarely able to resolve these scales directly, a variety of parameterizations for submesoscale dynamics have been developed.

An important diagnostic variable that provides insight into submesoscale motions is PV

$$\mathrm{PV} = \omega_a \cdot \nabla b, \tag{1}$$

where $\omega_a = f + \nabla \times \mathbf{u}$ is the absolute vorticity, expressed as the sum of the planetary and local vorticities, $b = g(1 - \rho/\rho_0)$ is the buoyancy, g is gravity, ρ is potential density, $\rho_0 = 1,025$ kg/m^3 is a reference density, and $\mathbf{u} = (u, v, w)$ are velocities in the (x, y, z) direction. PV is conserved in the absence of diabatic effects, such as wind stress or surface buoyancy forcing at the ocean surface, implying that once a fluid parcel subducts out of the mixed layer its PV is fixed.

If we assume terms associated with the gradient of the vertical velocity w are small, equation (1) becomes

$$\mathrm{PV} = (f + \zeta)b_z + u_z b_y - v_z b_x, \tag{2}$$

where $\zeta = v_x - u_y$ is the local vertical vorticity and subscripts denote partial derivatives. Assuming thermal wind balance, $(u_z, v_z) = (-fb_y, fb_x)$. Substituting $N^2 = b_z$ and $M^2 = \left(b_x^2 + b_y^2\right)^{1/2}$ as the squared vertical and horizontal buoyancy frequencies, respectively, results in

$$\mathrm{PV} = fN^2 + \zeta N^2 - f^{-1}M^4. \tag{3}$$

The first term is generally positive (in the Northern Hemisphere, where $f > 0$). The second term can take either sign and is responsible for the asymmetry in submesoscale dynamics between cyclonic ($\zeta > 0$) and anticyclonic ($\zeta < 0$) eddies (Brannigan et al., 2017; Rudnick, 2001). The third term is always negative (where $f > 0$) and can become large in frontal regions.

We use the framework of buoyancy gradients and PV to review three types of submesoscale instabilities: baroclinic instability within the mixed layer, gravitational instability (GI), and symmetric instability (SI). In section 5 we return to this framework to estimate the potential for each type of instability to export fixed carbon out of the surface ocean.

2.1. Mixed Layer (Baroclinic) Instability

Baroclinic instability occurs due to the release of potential energy stored in lateral density gradients. Baroclinic instability energizes submesoscale motions within the mixed layer (where it is sometimes called mixed layer instability; MLI), where surface buoyancy forcing or lateral stirring by mesoscale eddies causes strong horizontal buoyancy gradients to develop. MLI slumps steep isopycnals associated with large lateral density gradients, releasing potential energy by converting horizontal buoyancy gradients b_x into vertical gradients b_z, generally over a period of days (Boccaletti et al., 2007; Haine & Marshall, 1998). This overturning of density surfaces always acts to restratify the water column and can be expressed in terms of a vertical stream function

$$\psi_{\mathrm{MLI}} = 0.06\frac{\mu(z)b_x\mathrm{MLD}^2}{|f|}, \tag{4}$$

where $(u, w) = (\psi_z, -\psi_x)$, for z increasing upwards (Fox-Kemper et al., 2008). The term

$$\mu(z) = \left[1-(1-2z')^2\right]\left[1+\frac{5}{21}(1-2z')^2\right], \tag{5}$$

where $z' = z/\mathrm{MLD}$, is a vertical structure function that goes to 0 at the surface and base of the mixed layer, following a *no-normal-flow* condition at the boundaries of the mixed layer, which is assumed to be bounded by a highly stratified pycnocline at its base (Fox-Kemper et al., 2008)

MLIs have been implicated in initiating both small-scale (Lacour et al., 2017) and large-scale (Mahadevan et al., 2012) restratification-driven blooms, as well as driving submesoscale subduction of POC (Omand et al., 2015). However, their ability to, by themselves, subduct material out of the mixed layer is limited. As they are normally parameterized (e.g., Fox-Kemper et al. (2011), Gent et al. (2011), Hurrell et al. (2013), Tjiputra et al. (2013), Danabasoglu et al. (2014)), MLIs have no signature below the MLD due to $\mu(z)$, which is equivalent to assuming that the base of the mixed layer is a solid boundary. We will return to this assumption in section 5, where we discuss the implications for export through MLI of a mixed layer with weak stratification at its base.

MLIs can also lead to subduction and export when combined with diabatic processes, such as spring restratification driven by positive atmospheric heat flux. In this scenario, MLI subducts material from the surface to the base of the mixed layer, and another process, such as atmospheric buoyancy or Ekman forcing (see below), forms a new mixed layer above the now-subducted material. The export potential of this mechanism is, however, dependent on the definition of export used. Unless this capping of the mixed layer is associated with a downwelling regime (leading to mode water formation) or death and sinking of phytoplankton, this material will simply be reentrained into the mixed layer during the next mixing event.

2.2. Gravitational Instability

Gravitational instability (GI) releases potential energy in statically unstable density profiles ($b_z < 0$). GI is an integral part of the seasonal cycle, as surface cooling during the autumn and winter deepens mixed layers. Conversely, spring surface heating increases b_z and contributes to a stable restratification of the mixed layer. GI can also arise when the surface wind stress interacts with horizontal surface buoyancy gradients. If a component of the wind stress is perpendicular to the horizontal buoyancy gradient, surface Ekman transport will advect dense water over light if the wind stress is in the same direction as the geostrophic flow and vice versa if it is in the opposite direction (Thomas & Lee, 2005). As with surface buoyancy forcing, Ekman-driven gravitational effects can either destabilize or restabilize a water column.

Surface buoyancy and Ekman forcing is directly related to the mixed layer, since the MLD is, to a large extent, determined by the depth upon which buoyancy and Ekman forcing act. Therefore, GI will not act to subduct water masses beneath the mixed layer, since by definition this will cause the mixed layer to deepen. Stratifying buoyancy or Ekman forcing can, however, trap water masses beneath a new, shallower mixed layer and indirectly lead to export, as mentioned in section 2.1.

2.3. Symmetric Instability

Symmetric instability (SI) is a shear instability that drives vigorous slantwise convection along isopycnals (Hoskins, 1974). It arises from the interaction between buoyancy and absolute momentum restoring forces in areas with strong horizontal buoyancy gradients and weak absolute momentum gradients. Diagnostically, a water column is symmetrically unstable when $f\mathrm{PV} < 0$ and $-1 < Ri_b < f/\zeta$, where $f^2N^2M^{-4}$ is the balanced

Richardson number (Thomas et al., 2013). Taylor and Ferrari (2009) used idealized nonlinear simulations to find that Kelvin-Helmholtz instabilities ultimately relieve SI by mixing high-PV waters from the pycnocline with low-PV waters from the SI-unstable mixed layer. The time scale for this process is on the order of hours.

Because SI is often associated with large b_x, water columns that are symmetrically unstable are also subject to MLI. The depth to which SI acts can be approximated as the deepest depth H for which

$$f\int_0^H \mathrm{PV}dz > 0 \tag{6}$$

(Bachman et al., 2017; see also Appendix 2 of Whitt et al., 2017). Here we calculate this value directly from equation (3), with the approximations already discussed. The end result of SI is to homogenize the PV above this depth to 0, at which point MLI acts on the remaining horizontal buoyancy gradients (Haine & Marshall, 1998).

3. Data

We use data primarily from glider observations in the Porcupine Abyssal Plain region of the northeast Atlantic Ocean (Figure 1a). The region is located between the subtropical and subpolar gyres, is far from boundaries, and has no major bathymetric features. It experiences springtime bloom dynamics fueled by nutrients input into the surface ocean mainly through wind stress-induced mixing during winter (Martin et al., 2010; Rumyantseva et al., 2015). Both the initiation of the springtime bloom and flux of particles from the surface boundary layer exhibit substantial interannual variability (Hartman et al., 2010; Lampitt et al., 2010), with peak bloom times ranging from March to June (Figure 2). The seasonal distribution of MLD is controlled primarily by the air-sea heat exchange, with cooling and mixed layer deepening in winter and warming and shoaling in summer, although advection of waters into the area is also significant (Damerell et al., 2016).

Five gliders were deployed in pairs from September 2012 to September 2013 near the Porcupine Abyssal Plain site, with deployment times ranging from 2 to 5 months (Figure 1b and Table 1), as part of the Ocean Surface Mixing, Ocean Submesoscale Interaction Study (OSMOSIS). For the purposes of this paper, we define gliders SG502 and SG566 as *Glider 1* and SG510, SG533, and SG579 as *Glider 2* (Figure 1b and Table 1). Thompson et al. (2016) and Buckingham et al. (2016) show evidence of seasonality in submesoscale turbulence from the gliders and from moorings deployed over the same time period, respectively. Here we consider the connection between submesoscale dynamics, productivity, and the potential for export in this region.

The gliders were piloted in bow tie-shaped paths within a 20×20 km region of the ocean centered at 48.7°N, 16.2°W (Figure 1c). Dives were V-shaped to 1-km depth, with 3–5 hr and 2–4 km between surfacings, or about a day per leg of each of the transects. The gliders all carried unpumped CTD sensors measuring conductivity (salinity), temperature, and depth (pressure) at a vertical resolution of less than 1 m. Calibration of glider sensors is typically done using ship-based profiles at deployment and recovery (as in Damerell et al., 2016). The advantage of this method is the high confidence in ship-based sensors, which can themselves be calibrated before, after, and during the cruise. A disadvantage is the lack of calibration measurements during the glider deployment, which can be important if a sensor starts to drift middeployment or if time considerations, inclement weather, or sensor malfunction prohibits calibration measurements during deployment or recovery (as happened for the first recovery of SG533; see Table 1). Instead, we perform an interglider calibration, which capitalizes on the overlap in glider deployments. Specifically, average temperature and salinity values with respect to depth were compared across glider platforms over time intervals when both were in the water. Sensor drifts were not observed, but depth-dependent offsets of salinity and temperature for individual gliders were required, of up to 1 PSU and 0.06 °C, respectively.

In addition to the physical measurements, each of the gliders carried an Aanderaa oxygen optode and WET Labs sensors for induced fluorescence (hereafter, fluorescence) and optical backscatter (hereafter, backscatter) at various wavelengths (Table 1). Oxygen and WET Labs measurements were taken roughly every 1–2 m in the vertical to depths between 200 and 500 m, although occasional profiles to the full depth of 1 km were also taken to retrieve the background signal. Oxygen measurements were calibrated against ship-based oxygen measurements before and after each cruise, which were themselves calibrated with Winkler titration of water samples (Binetti, 2016). The gliders also carried PAR (Photosynthetically Available Radiation) sensors (400–700 nm), which were used by Hemsley et al. (2015) to calculate productivity, and all but one glider had

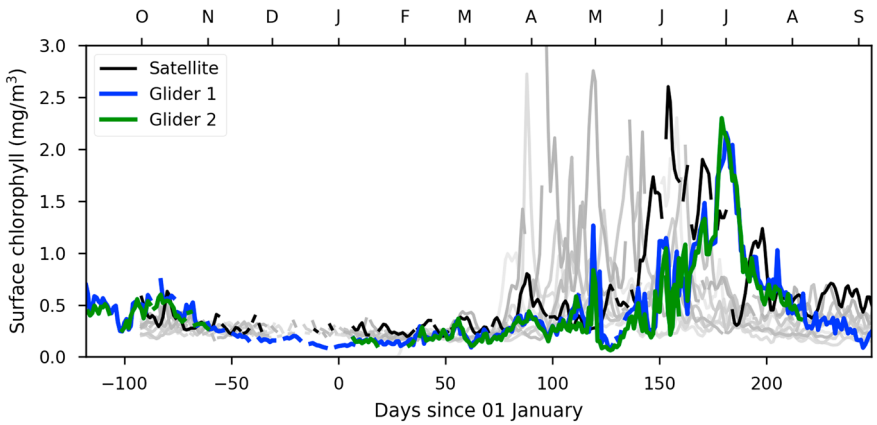

Figure 2. Average surface chlorophyll concentrations each year from 2002–2003 to 2011–2012 from MODIS Aqua (gray lines, chronologically light to dark) using the region within the dashed black box in Figure 1a. Thick black line is from 2012–2013, which covers the OSMOSIS study period; blue and green lines are the average data in the upper 25 m, after calibration, for Gliders 1 and 2, respectively (see section 3 and Table 1). MODIS = Moderate Resolution Imaging Spectroradiometer; OSMOSIS = Ocean Surface Mixing, Ocean Submesoscale Interaction Study.

a CDOM (Colored Dissolved Organic Material) sensor. The CDOM measurements were largely within the noise range for the sensor and contained instrument effects related to the sampling frequency, for which we are at present not able to correct. We therefore do not consider the CDOM data further in this paper.

Fluorescence and backscatter data are often used as proxies for chlorophyll concentration (e.g., Boss et al. (2008)), but care must be taken in interpreting them as such. Fluorescence measures the potential productivity of the water sample (Daly et al., 2004) and is typically scaled to a chlorophyll concentration using laboratory measurements of a diatom monoculture (*Thalassiora weissflogii*) after accounting for a linear offset (dark counts). A major difficulty in converting fluorescence to chlorophyll concentrations is in correcting for nonphotochemical quenching, defined as the sum of all processes that reduce fluorescence in high-light conditions as a protection mechanism for the light-harvesting apparatus (Cullen & Lewis, 1995). A common correction algorithm makes use of backscatter data and a known ratio between backscatter and fluorescence in areas not affected by nonphotochemical quenching (Boss et al., 2008). Self-shading by phytoplankton in the water column can also be measured by a PAR sensor and used to correct for low fluorescence values (Hemsley et al., 2015; Xing et al., 2011). Because we use a long time series and some of our results concern changes in the fluorescence to backscatter ratio, we circumvent the issue by using only nighttime fluorescence data.

Laboratory-based estimates of dark counts are rarely consistent with the in situ instrument response, so here we determine the dark counts for each glider as the median of all measurements below 600 m depth for each glider deployment (for the first deployment of SG533, we instead use measurements below 280 m because no

Table 1
Biological Sensor Packages (WET Labs ECO Puck) for Each Glider Deployment

Seaglider		Deployment dates		Backscatter wavelength		Chlorophyll calibration	
ID	#	Start	End	Sensor 1	Sensor 2	Scale factor	*n*
SG502	1	08 Jan 2013	23 Apr 2013	470 nm	700 nm	1.9	17
SG510	2	19 Apr 2013	09 Jun 2013	650 nm	—	4.1	9
SG533	2	06 Sep 2012	08 Jan 2013[a]	650 nm	—	3.2	7
	2	03 Jun 2013	05 Aug 2013	650 nm	—	2.8	10
SG566	1	04 Sep 2012	08 Jan 2013	650 nm	—	3.1	11
	1	19 Apr 2013	07 Sep 2013	650 nm	—	3.1	26
SG579	2	08 Jan 2013	23 Apr 2013	532 nm	—	2.2	14

Note. Seaglider # refers to its designation in Figure 1b. Scale factor is the multiplicative factor between MODIS Aqua and glider observations, where *n* is the number of MODIS Aqua observations used to calculate the scale factor. MODIS = Moderate Resolution Imaging Spectroradiometer.
[a]Issues with the temperature sensor rendered conductivity-temperature-depth data unusable after 4 November.

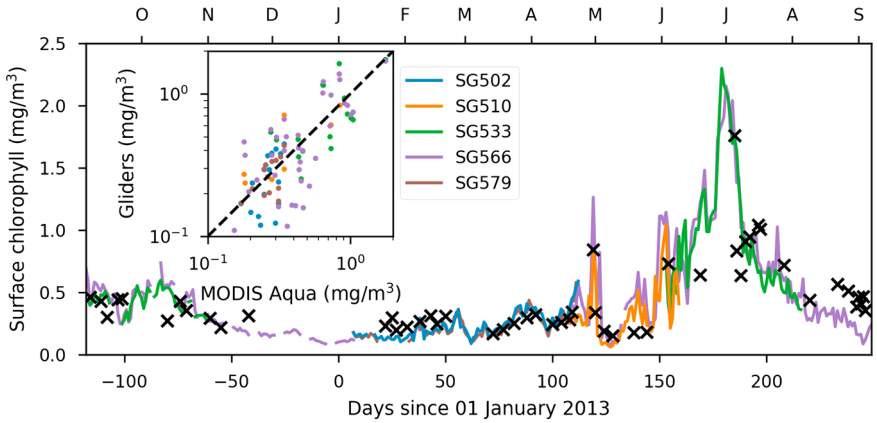

Figure 3. Surface chlorophyll data from each glider averaged over the upper 25 m during nighttime (colors), after calibrating with MODIS Aqua overpasses (black crosses; see Table 1 for scaling factors). Inset scatters calibrated glider measurements against MODIS Aqua results, where the dashed black line is 1:1. MODIS = Moderate Resolution Imaging Spectroradiometer.

measurements deeper than 300 m were taken). In so doing, we make the assumption that fluorescence below this depth (well below the euphotic zone) is negligible. Fluorescence profiles often show abrupt spikes, which may be due to aggregated material (Briggs et al., 2011). We filter out these spikes using a five-point minimum followed by a five-point maximum filter (similar to the method used in Briggs et al. (2011)). The spike signal shows no structure, and here we only consider the filtered (baseline) signal.

Recent results have shown that factory-calibrated ECO Puck sensors' measurements of chlorophyll are greater than in situ chlorophyll measurements by a factor of 1–6 (Roesler et al., 2017). We determine this scaling factor by comparing daily average (nighttime) surface measurements in the upper 25 m with estimates of chlorophyll from the nearest Moderate Resolution Imaging Spectroradiometer (MODIS) Aqua measurement (OC3 algorithm; Level 3 gridded product at 4-km resolution) and obtain factors comparable to Roesler et al. (2017; Table 1). Using satellite data rather than ship-based measurements allows calibration throughout the deployment, which might span several ecological regimes. However, additional uncertainty is introduced because satellite chlorophyll concentration estimates are less reliable than ship-based laboratory measurements. We compare our calibrated Seaglider data with MODIS Aqua estimates (crosses) in Figure 3, where the inset shows a scatterplot of the observations after calibration. The relatively small number of comparisons

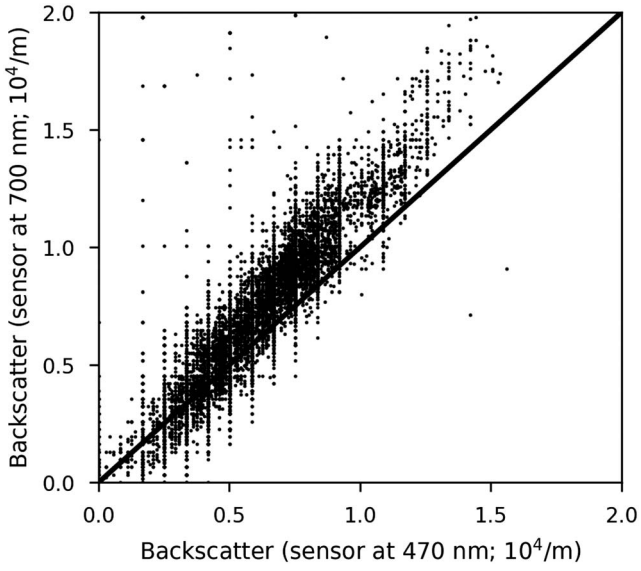

Figure 4. Scatterplot of coincident backscatter measurements at 470 and 700 nm from SG502 after offset, despiking, and calibration using a wavenumber slope of k^{-1} as described in the text. The ideal 1:1 line is shown in black.

is due to frequent cloud cover in this region. Substantial scatter still exists in the calibration, but this scatter is relatively evenly distributed about the 1:1 line (inset). Much of this can be explained because of the comparison between point measurements by the gliders and average measurements over an approximately 1 km^2 footprint by MODIS Aqua. In addition, up to 12 hr can separate the nighttime glider observation from the satellite measurement, which has a local overpass time between 13:00 and 15:00. Jacox et al. (2015), however, showed that calibration measurements can be effective tens of kilometers and many days distant from the in situ observation.

Backscatter data are from sensors with wavelengths ranging from 470 to 700 nm. We offset for dark counts using the same procedures as for fluorescence. In this case, finding an offset as the median value below a certain depth is less well justified. Backscatter presented here is thus more accurately the difference in backscatter from a bulk interior value. In order to treat all wavelength sensors equally, we convert to an equivalent measurement at 650 nm assuming a k^{-1} slope of backscatter with respect to wavelength (Boss et al., 2008). We test this relationship using SG502, which was equipped with backscatter sensors at 470 and 700 nm. The observations after assuming a k^{-1} slope lies close to a 1:1 line between the two sensors (Figure 4), with a best fit slope of $k^{-0.92}$. The remaining scatter can be understood as a combination of noise and differences in water masses from the two sensors pointing in different directions. (Note that the preferential values for backscatter at 470 nm, at intervals of approximately 10^{-5} m^{-1}, are due to the discreteness of the underlying data set.)

4. Results

4.1. Seasonality of Chlorophyll and Community Index

Chlorophyll concentrations are confined to the mixed layer, defined here as the depth at which the density increases by 0.03 kg/m^3 over the density at 10 m depth (de Boyer Montégut et al., 2004), except when the mixed layer is shallow, in which case high-chlorophyll waters extend to the depth of the euphotic zone at 50–100 m (Hemsley et al., 2015; Figure 5a). Maximum values of chlorophyll ($\sim$ 4 mg/m^3) exist near the surface in June and July. However, small chlorophyll concentrations persist within the mixed layer throughout winter (note the logarithmic colorbar). The surface average chlorophyll concentration (upper 25 m) is shown in panel b, as well as the integrated upper ocean chlorophyll (in the upper 500 m). Sporadic short-lived surface blooms occur throughout the winter, coincident with abrupt shoalings of the mixed layer. The final restratification event in April and May kicks off the spring bloom. After an initial burst of photosynthetic activity at the surface, chlorophyll concentrations are consolidated primarily within a subsurface chlorophyll maximum just below the MLD, and production is maximized near the MLD (Hemsley et al., 2015). Although the gliders did not measure nutrient concentrations, this is consistent with an early depletion of surface nutrients followed by subsequent production at the nutricline, located slightly below the pycnocline.

The surface backscatter data are similar to that of fluorescence (Figure 5c), showing a dominant peak in June–July and smaller peaks in previous months. The interior backscatter concentrations, however, show a marked increase from December through mid-April, spanning multiple glider deployments (Figure 5d). If we assume a specific relationship between backscatter and POC, this could be interpreted as a buildup of POC over the winter months. However, since we do not have in situ calibration for any backscatter to POC conversion, we choose to work with the glider-derived backscatter measurements and focus our analysis on relative changes in this quantity.

4.2. Community Composition

The composition of phytoplankton species is important in determining export potential, as the remineralization coefficient of aggregates varies widely (Armstrong et al., 2002; Berelson, 2001). Field experiments characterizing phytoplankton composition in this region have found a short-lived surface diatom bloom that evolves into a subsurface chlorophyll maximum dominated by diatoms during early summer (Painter et al., 2010). A simple ratio of fluorescence to backscatter, also known as the optical *community index*, is shown in Figure 6a. Cetinić et al. (2015) used this ratio to categorize phytoplankton species, with larger diatoms having a higher ratio than smaller picophytoplankton. We expect diatoms to flourish under high-nutrient conditions, such as during the springtime bloom and at the nutricline in the summer. While the community index approach does not take into account many other biological effects, the results from this simple analysis agree with expectations: high values (greens) where we expect high nutrients; midrange values (reds) where nutrients are scarce, such as during autumn and at the surface in summer; and low values (blues) where we expect no production (below mixed and euphotic layers).

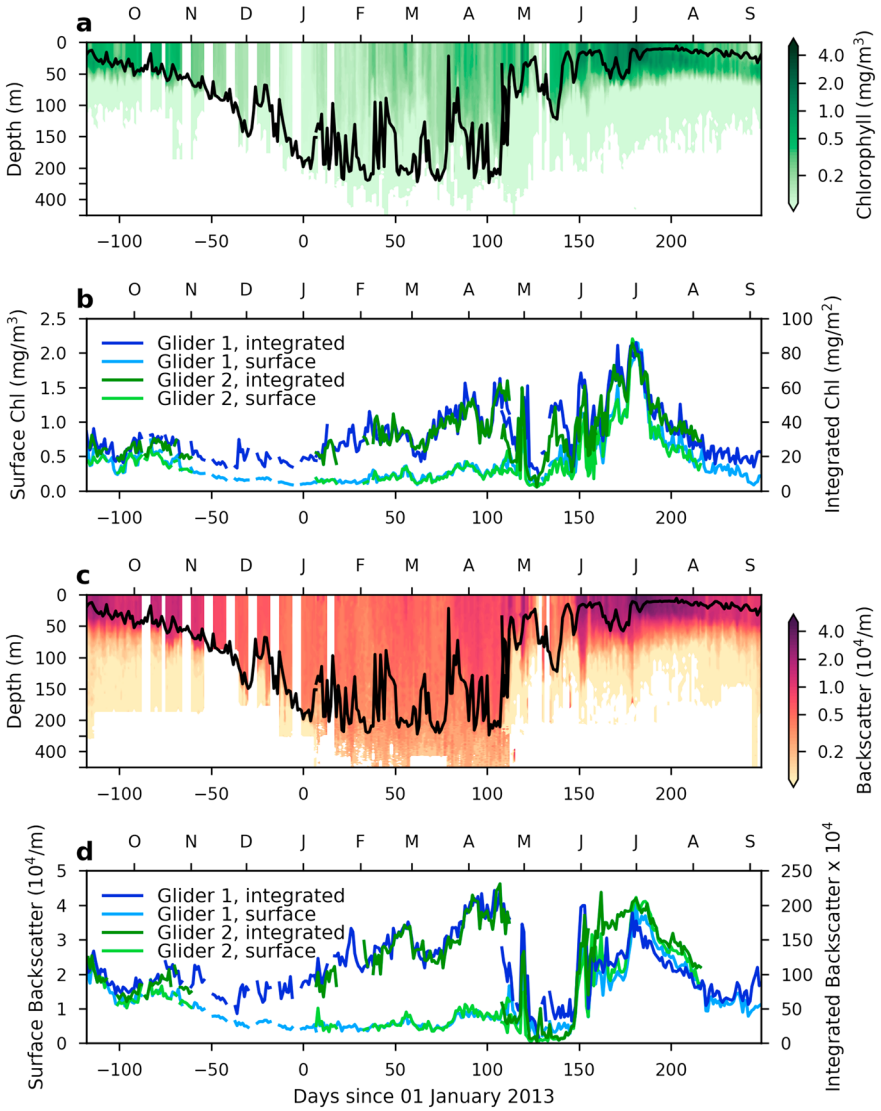

Figure 5. (a) Nighttime chlorophyll concentrations in the upper 500 m (note change in vertical scale at 200 m). (b) Average surface (upper 25 m) chlorophyll concentrations (blue) and total (upper 500 m) chlorophyll concentrations (green). (c, d) As in panels a and b, except for backscatter at 650 nm (see text). Black lines in (a, c) give the mixed layer depth.

The community index convolves information on community composition with other processes, such as photoacclimation, which can impact the amount of chlorophyll per unit biomass. Photoacclimation increases the concentration of chlorophyll and accessory pigments under low light conditions and acts on a time scale of under a day (Neori et al., 1984). During the spring, the community index within the mixed layer is correlated with the MLD on short time scales (Figure 6b). For example, the deepening event in June is accompanied by increased fluorescence:backscatter ratios, consistent with the effects of photoacclimation. However, another mechanism potentially at work is an entrainment of nutrients into the mixed layer during mixed layer deepening events, which promote the growth of large species such as diatoms with high fluorescence:backscatter ratios.

4.3. Seasonality of PV and AOU

In Figure 7a we show PV in the upper 500 m of the water column for Glider 1. In calculating PV through equation (3), we take u and x to be the velocity and direction, respectively, along the glider path. One-dimensional glider transects give no information about derivatives in y. One option is to assume $b_x = b_y$.

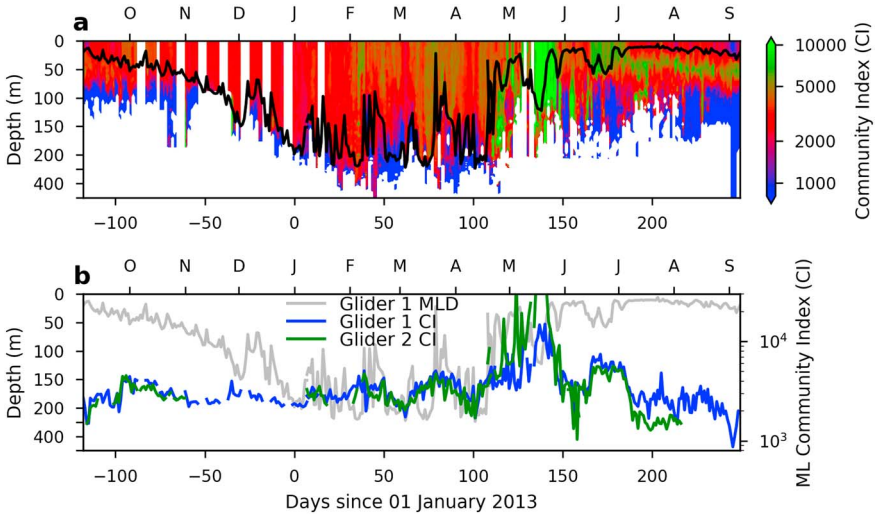

Figure 6. (a) Community index, defined as the ratio of chlorophyll to backscatter, in the upper 500 m (note change in vertical scale at 200 m). (b) Average ratio of chlorophyll to backscatter within the mixed layer. Black line in (a) and gray line in (b) show the mixed layer depth. MLD = mixed layer depth; CI = community index.

In an approximately horizontally isotropic region such as is considered here, this approximation yields accurate average PV values. However, assuming $b_x = b_y$ increases the number of negative PV events beyond what is actually present. We instead conservatively approximate $b_y \equiv 0$, $M^2 \approx b_x$, and $\zeta = v_x$. This is likely to bias our final PV estimates positive and identify fewer negative PV events than actually occurred (see detailed discussion and analysis in Thompson et al. (2016)).

The waters above the MLD (thick black line) are low in PV (blue colors), reflecting primarily low vertical buoyancy stratification within the well-mixed part of the ocean. The base of the mixed layer is host to a strongly stable pycnocline (red colors) during June–November. During December the pycnocline erodes. Here we calculate the MLD using a threshold method of 0.03 kg/m^3 difference in density from the density at 10 m depth (de Boyer Montégut et al., 2004), which defines a wintertime mixed layer of 100–250 m. This definition is consistent with the chlorophyll concentrations, which become near 0 beneath this depth (Figure 5a). MLD calculated by this definition is also very similar to MLD calculated by a vertical density gradient of 5×10^{-4} kg/m^4 (not shown; Dong et al., 2008). However, the MLD is highly sensitive to the precise definition of mixed layer used, and it may be more accurate to say that the base of the mixed layer is no longer well defined, because of the lack of a strong pycnocline within the upper water column.

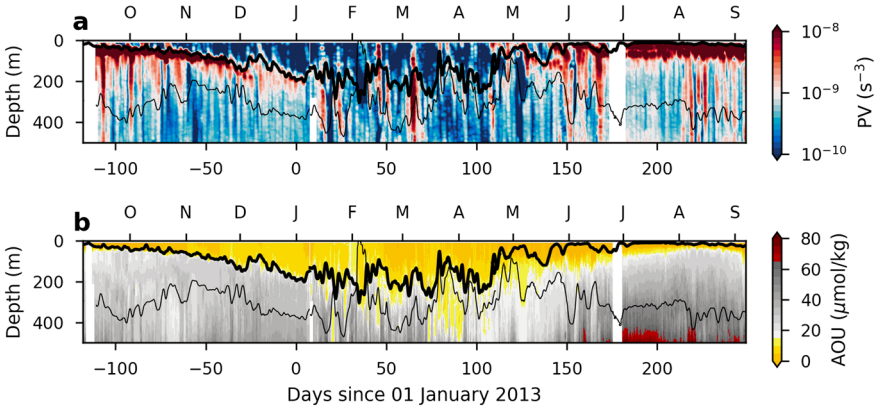

Figure 7. (a) PV, calculated as in equation (3), and (b) AOU, calculated as the difference between saturated and measured oxygen concentrations, from Glider 1. Thick black lines give the MLD, and thin black lines give the $\sigma_0 = 27.1$ kg/m^3 isopycnal. PV = potential vorticity; AOU = apparent oxygen utilization; MLD = mixed layer depth.

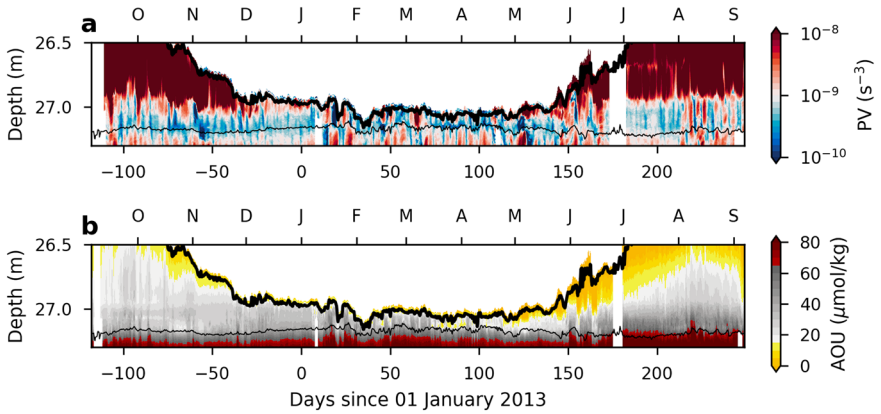

Figure 8. As in Figure 7, but on potential density surfaces rather than depth. Thick black lines give the MLD, and thin black lines are the 500 m isobar. PV = potential vorticity; AOU = apparent oxygen utilization; MLD = mixed layer depth.

The interior of the ocean below the pycnocline is also relatively low in PV. Isolated pockets of waters with very low PV are also present, the most prominent being at 100–300 m depth in early May. Since PV is conserved in the absence of frictional effects, we expect that these low-PV waters were subducted from the mixed layer.

We test the hypothesis that low-PV waters were subducted from the mixed layer using apparent oxygen utilization (AOU), the difference between saturated and measured oxygen concentration. AOU decreases with photosynthesis and increases with respiration, and is reset to 0 when a water parcel comes in contact with the atmosphere. Thus, low (high) AOU values are characteristic of water that has (has not) been recently ventilated at the surface. AOU values are near 0 at the surface and within the mixed layer and decrease slightly due to photosynthesis during the spring bloom in May–July (Figure 7b). AOU tends to increase with depth but is low where PV is low, which suggests that these low-PV waters below the mixed layer have indeed been recently subducted.

Low-AOU waters (yellow colors) are found within the mixed layer from summer through early winter (September–January) but exist below the MLD in late winter and spring (February–June). Figure 8 shows PV and AOU on potential density rather than depth surfaces (to relate the two, the thin black line in Figure 7 is the 27.01 kg/m^3 isopycnal, and the thin black line in Figure 8 is the 500 m isobar). Low PV values align along the 27.0–27.25 kg/m^3 potential density surface, which is also the density of the mixed layer during winter. AOU values in this same potential density range decrease suddenly in the wintertime and then slowly increase over time in the spring and summer. This increase of approximately 20 μmol/kg over 100 days is, however, much faster than typical oxygen utilization rates (Sarmiento et al., 1990), signifying the importance of horizontal advection (Damerell et al., 2016; Hartman et al., 2010). These results show subduction of passive tracers such as AOU during winter and motivate the need for a better understanding of how these subduction processes interact with surface biological variables such as chlorophyll and backscatter.

4.4. External Forcing and Submesoscale-instability Export

An increase in sea surface temperature is associated with the spring restratification in MLD but occurs well after the atmospheric heat flux becomes positive, indicating that surface heat flux is not the only factor contributing to the restratification (Figures 9a and 9b). The wind stress (τ) decreases throughout the spring from a maximum in winter. Increasing (decreasing) τ will deepen (shoal) the mixed layer, and indeed short-lived deepenings of the mixed layer in May and June correspond to increases in τ (Figure 9a).

Brannigan (2016) and Brannigan et al. (2017) predict that symmetric instabilities will be strongest near the periphery of anticylonic eddies. We use sea level anomaly measurements from AVISO (Archiving, Validation and Interpretation of Satellite Oceanographic data), where positive (negative) values of sea level anomaly correspond to cyclones (anticylones; Figure 9c, black). The Okubo-Weiss parameter (OW) is shown in gray in Figure 9c, where

$$\mathrm{OW} = S_n^2 + S_s^2 - \zeta, \tag{7}$$

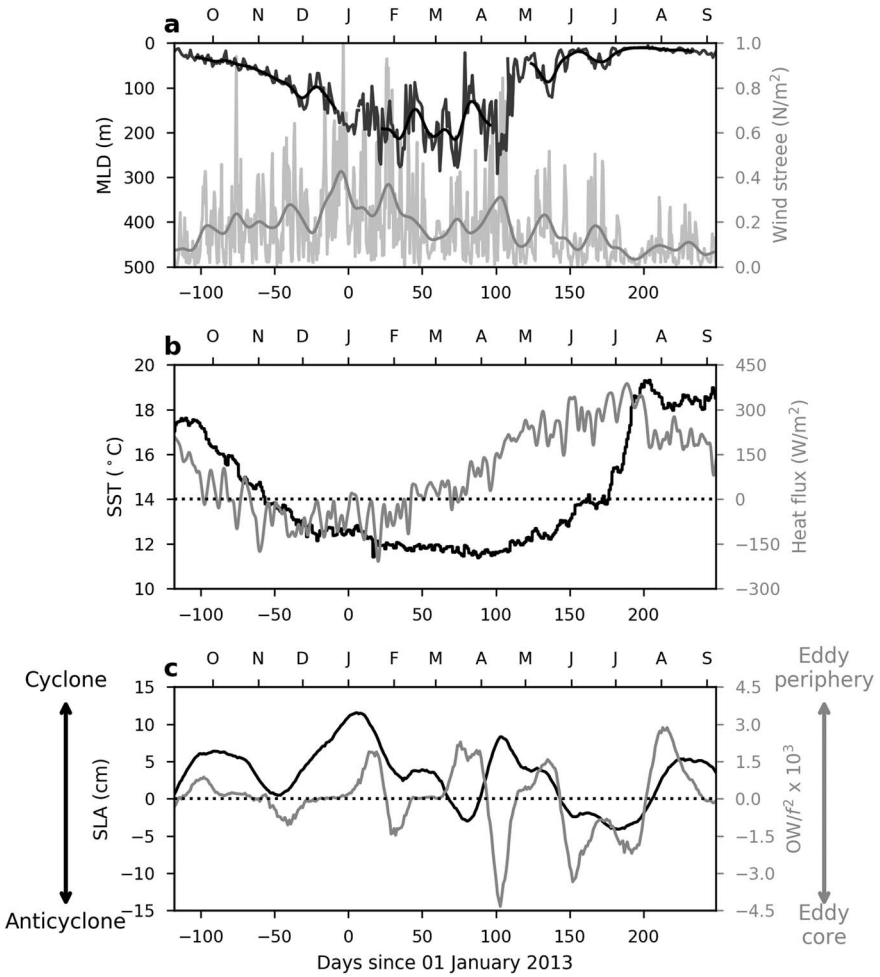

Figure 9. (a) MLD (dark gray) from Glider 1, and after filtering with a Gaussian window (standard deviation of 1 day; black). Wind stress (light gray) and after filtering with a Gaussian window (standard deviation of 1 day; gray). (b) SST (black) and total heat flux from the atmosphere (gray), both filtered with a Gaussian window with standard deviation of 1 day. (c) SLA (black) and the OW (equation (7)) scaled by f (gray). Wind stress, SST, and total heat flux from ECMWF ERA-Interim reanalysis are shown as an average for values within a 1° by 1° box centered on the OSMOSIS location. SLA and OW from AVISO data at the pixel nearest the OSMOSIS location. MLD = mixed layer depth; SST = sea surface temperature; SLA = sea level anomaly; OW = Okubo-Weiss parameter; ECMWF = European Centre for Medium-Range Weather Forecasts; ERA = ECMWF Re-Analysis; OSMOSIS = Ocean Surface Mixing, Ocean Submesoscale Interaction Study; AVISO = Archiving, Validation and Interpretation of Satellite Oceanographic data.

where $S_n = u_x - v_y$ and $S_s = v_x + u_y$ are the normal and shear components of strain. Regions in the center (periphery) of an eddy will have strongly negative (positive) OW (Henson & Thomas, 2008). Due to the low resolution (1/4°) of AVISO data, $|\mathrm{OW}| \ll f^2$; however, in reality, strong eddies will be associated with $|\mathrm{OW}|/f^2 \sim 1$. The OSMOSIS location encounters three prominent eddies (days 0–40, 90–110, and 150–200) throughout the year, of which the first two are cyclonic and the third anticyclonic. Smaller-scale eddies not captured by AVISO are likely also present.

A pronounced low-PV subduction event occurs in early May (Figure 7), when the OSMOSIS region is in the periphery of a cyclonic eddy. Figure 10 shows PV, AOU, and chlorophyll concentration for this event. The subduction feature is bounded by potential density surfaces at 27.09 and 27.1 kg/m^3 (thin black lines). A subduction signal is clearly indicated in decreased PV and AOU but is not present in the chlorophyll data (or backscatter; not shown), suggesting that this event did not correspond with export of fixed carbon out of the surface ocean.

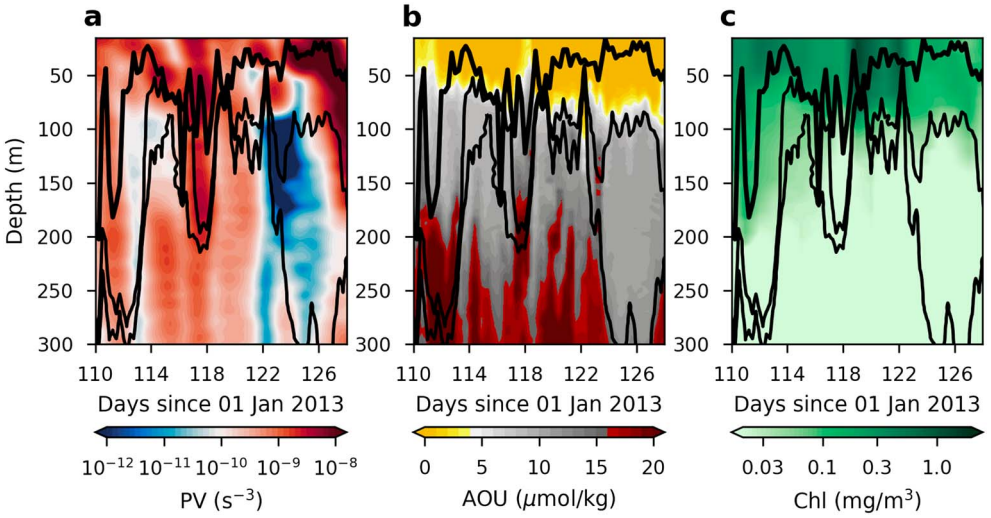

Figure 10. PV (a), AOU (b), and chlorophyll (c) from SG566 from 20 April to 8 May. Thick black line gives the MLD; thin black lines show isopycnals at 27.09 and 27.1 kg/m^3. PV = potential vorticity; AOU = apparent oxygen utilization; MLD = mixed layer depth.

5. Discussion

5.1. Event-Level Export

Which of the submesoscale instabilities outlined in section 2, if any, are responsible for the subduction events observed over the winter period? The vertical velocity w_{MLI} associated with MLI (from equation (4)) for the time period before and during that shown in Figure 10 is given in Figure 11a. Large vertical velocities (> 20 m/day) associated with MLI are present throughout wintertime but, by definition, go to 0 at the base of the mixed layer. This no-normal-flow boundary condition at the mixed layer depth is due to the $\mu(z)$ term (equation (5)), which goes to 0 at the top and bottom of the mixed layer.

The characteristic depth over which turbulence occurs during an SI event is given by H, as determined through equation (6), and is plotted in Figure 11b (blue line). As discussed in section 2.3, H is the depth over which mixing must occur to bring PV back to marginal stability, that is, PV = 0. The depth at which GI, or convection, occurs is given by the convective depth h (Figure 11b, red line) and is always less than H. The convective depth is solved using the quartic equation

$$\left(\frac{h}{H}\right)^4 - 14^3\left(1-\frac{h}{H}\right)^3\left[\frac{w_*^3}{|\Delta u_g|^3}+\frac{u_*^2}{|\Delta u_g|^2}\cos\phi\right]^2 = 0, \tag{8}$$

where $h \le H$, $w_* = (B_0 H)^{1/3}$ is the convective velocity; $u_*^2 = \sqrt{|\tau|/\rho_0}$ is the friction velocity; τ is the surface wind stress; $B_0 = F\alpha g C_p^{-1}\rho_0^{-1}$ is the surface buoyancy flux; ϕ is the angle between the wind vector and the geostrophic shear, which in this case is the glider orientation; F is the total heat flux; α is the thermal expansion coefficient; C_p is the specific heat of seawater; and Δ refers to the difference between the surface and $z = H$ (Taylor & Ferrari, 2010; Thomas et al., 2013). As GI is a diabatic process, a convective depth $h >$ MLD will result in mixed layer deepening and entrainment of new material into the mixed layer, while retaining surface tracers such as phytoplankton in the well-mixed region. Thus, $h >$ MLD is only possible transiently before the mixed layer responds by deepening. Sporadic events occur where GI extends below the MLD (Figure 11b); we assume that these are associated with a deepening of the mixed layer and that GI does not contribute to export production.

Theoretically, surface buoyancy gain can form a new, shallow mixed layer that overlays a deeper, denser mixed layer. This capping effect can lead to export either through large-scale advection of this remnant water mass to deeper depths or slow sinking of particles in this water mass (Carlson et al., 1994). At the OSMOSIS site, however, this effect does not seem to be dominant, as the major mixed layer shoaling events in April and May do not leave behind high-chlorophyll or high-backscatter waters (Figures 5a and 5c).

The SI depth H, however, often reaches below the MLD, and indeed a SI event takes place shortly before the most prominent subduction feature observed during the OSMOSIS time series (Figure 10). This points to SI

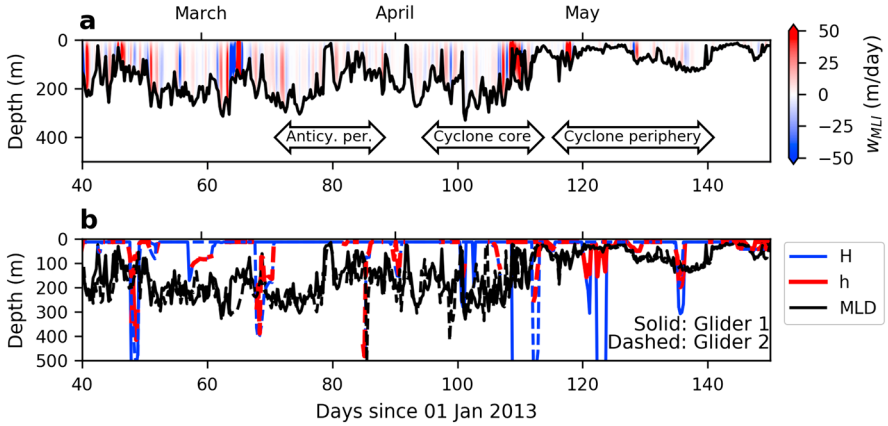

Figure 11. (a) Vertical velocity $w = -\psi_x$ (equation (4)) associated with mixed layer instability, with positive w indicating upwelling. (b) Depths at which the water column is symmetrically unstable (H, blue line; equation (6) and gravitationally unstable (h, red line; equation (8). Solid (dashed) lines are from Glider 1 (2). Black lines in each panel give the mixed layer depth. MLI = mixed layer instability; MLD = mixed layer depth.

as a primary candidate for export across the base of the mixed layer. The limited duration of the extreme H values shown in Figure 11b reflects the relatively short temporal and spatial scales over which SI events occur. This highlights the difficulty in observing SI, as these instabilities are quickly stabilized. MLI tends to occur over a longer time scale of days, but from the snapshot nature of the glider observations, it can be difficult to determine the stage of the instability. It is important to note that the diagnostics presented here provide a statistical representation of the submesoscale motions that are active in this region but do not capture the life cycle of any individual instability process.

SI could give rise to the observed subduction features seen here (e.g., Figure 10), as it provides a clear mechanism for export below the mixed layer through entrainment of pycnocline and other sub-mixed layer waters into the mixed layer. SI also occurs on time scales of order hours, meaning that the biological field can be well approximated as a passive tracer for this process, and the existence of symmetrically unstable waters extending below the mixed layer during winter is consistent with episodic injections of low-PV and low-AOU waters (Thompson et al., 2016), as is shown in Figures 10a and 10b. Unlike Brannigan (2016) and Brannigan et al. (2017), we do not observe a clear increase in SI events while the gliders are in the periphery of an eddy. However, the total number of events captured is small, so we cannot conclusively comment on this prediction.

Although SI is present during winter, MLI effects may also contribute to the subduction of mixed layer waters into the interior. At the OSMOSIS region, and in many other middle- to high-latitude regions, a well-defined mixed layer base does not exist during wintertime, and MLI can produce vertical velocities that extend across the base of the mixed layer. Callies et al. (2016) show that the vertical decay scale of a tracer anomaly with wavelength k due to MLI is kN/f. If N increases sharply at the MLD, this scaling drastically limits the vertical range at which MLI can extend below the mixed layer, but if N is small below the mixed layer, substantial vertical penetration is possible.

As described above, an important aspect of this system is the coupled seasonal cycle of MLD and the stratification at the base of the mixed layer, and in particular the difference in these properties across the fall-winter and winter-spring transitions (Figure 12a). During winter, mixed layers are deep and vertical stratification at the base is small. This is shown schematically in Figure 12b, where the along-isopycnal movement of water due to MLI is indicated by the gray arrows. The combination of deep mixed layers, implying a large reservoir of available potential energy, and weak stratification, causing a weak vertical decay of vertical velocities, can lead to deep subduction of water masses through MLI. During the spring, the mixed layer shoals, but periodic destratification events keep the vertical stratification at the base of the mixed layer weak, and along-isopycnal motions can still lead to deep subduction. During summer, a strong pycnocline forms, and the mixed layer is shallow with a well-defined base (Figure 12c). This is the type of mixed layer that is well parameterized by equation (4), with negligible export potential. Interestingly, during autumn the pycnocline is stronger than during spring (Figure 12a), limiting the potential for export during this season, even though the mixed layer is deepening and submesoscale motions in the mixed layer will be more energetic (Su et al., 2018). Thus, the

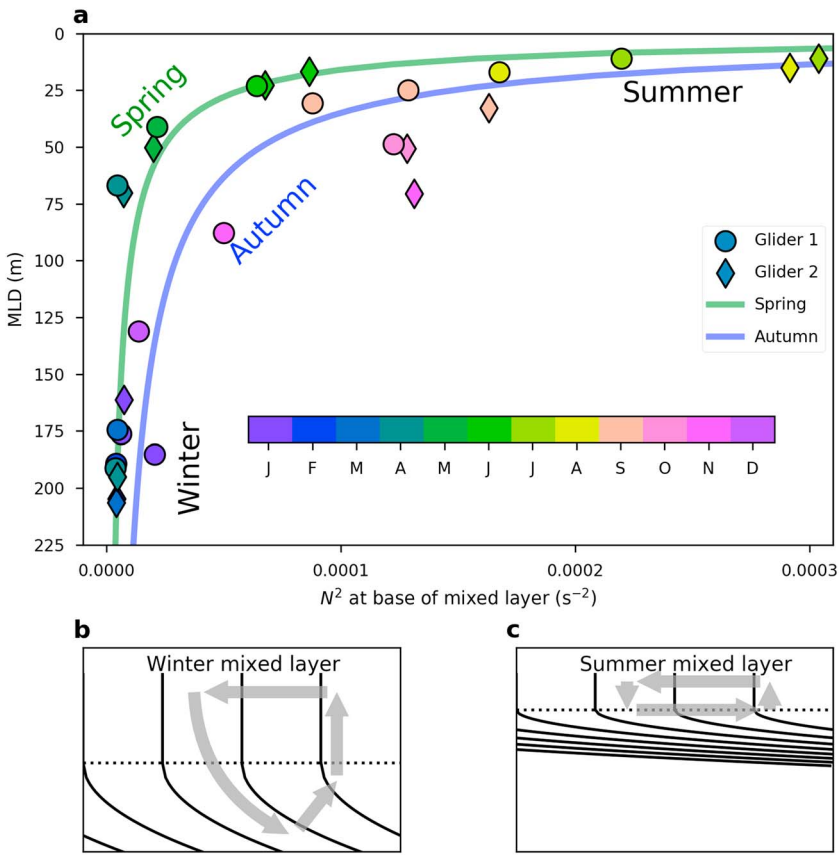

Figure 12. (a) MLD and vertical stratification at the base of the mixed layer as monthly averages for Glider 1 (circles) and Glider 2 (diamonds). The best fit exponential for the winter-to-summer (summer-to-winter) transition is shown in green (blue). (b, c) Schematics for winter (b) and summer (c) surface ocean densities, where solid lines are isopycnal surfaces, dotted lines are the mixed layer depths, and gray arrows show the effect of MLI. MLD = mixed layer depth; MLI = mixed layer instability.

vertical velocities at the base of the mixed layer, and particularly their decay into the interior of the ocean, need to be parameterized accurately based on the observed or simulated stratification to properly account for export by submesoscale motions.

5.2. Seasonal/Annual Export

There is increasing evidence that submesoscale motions are broadly active throughout the ocean and in particular in regions with strong spring blooms (e.g., the midlatitudes and subpolar gyre in the North Atlantic). Submesoscales are most active when mixed layers are deep, providing large reservoirs of available potential energy (Boccaletti et al., 2007; Su et al., 2018). The transition from deep to shallow mixed layer conditions can occur rapidly, on the order of 1 or 2 weeks, but the transition may have different timing and duration from year to year. In addition, transient restratification events, as seen in the MLD during winter in Figure 5, may induce small-scale blooms that can be exported when the mixed layer deepens and submesoscale motions are enhanced.

A schematic for the large-scale seasonal evolution of export from submesoscale instabilities is shown in Figure 13. In the winter, mixed layers (blue, top) are deep and highly variable. Stratification at the base of the mixed layer, $N^2|_{MLD}$, is small, reflecting a weak pycnocline (red, top). These conditions both lead to the potential for large vertical velocities at the base of the mixed layer $w|_{MLD}$ through the submesoscale instabilities discussed in this paper (blue, middle). The winter is therefore a time of large amounts of subduction out of the mixed layer.

Export, however, requires fixed carbon to be present. As discussed in section 1, bloom dynamics and POC concentrations are strongly inversely proportional to the MLD (Sverdrup, 1953); this is true in the OSMOSIS region as well, although we do show nonnegligible amounts of fluorescence and backscatter during winter

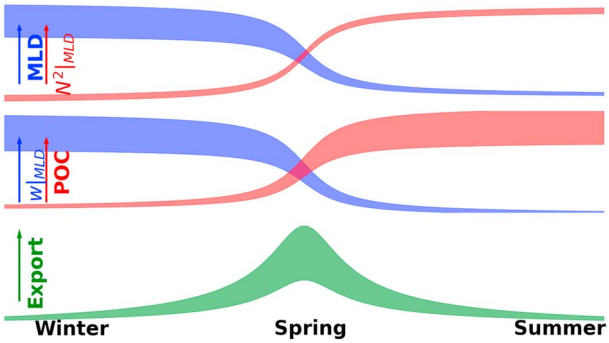

Figure 13. Schematic of the seasonal evolution of the MLD, the strength of the pycnocline (N^2 at the base of the mixed layer), the strength of vertical motions associated with submesoscale instabilities (w at the base of the mixed layer), POC concentrations, and export $\langle w'\mathrm{POC}'\rangle$ throughout the year. The width of the curves represents the expected variance in these properties throughout the seasonal cycle. The typical time scale of the spring transition is of the order of weeks, but the time of year can vary widely. MLD = mixed layer depth; POC = particulate organic carbon.

(Figures 5a and 5b). In the spring and summer, fixed carbon concentrations, represented here as POC, increase (red, middle). Export mediated by submesoscale instabilities (Omand et al., 2015), which can be calculated as $\langle w'\mathrm{POC}'\rangle$ (green, bottom), is therefore highly dependent on the temporal overlap between submesoscale vertical velocities and POC concentrations.

Our results here suggest that export rates due to physical processes at the OSMOSIS site in winter/spring of 2013 are low, although we do find evidence of subductive events. These observations are consistent with a relatively limited period of overlap between high vertical velocities and high POC concentrations. However, we emphasize that this study represents conditions at one particular location and one particular year. It would not be surprising to encounter different behavior in subsequent experiments, and there is clearly a need to find new ways to assess the overlap window between submesoscale instabilities and productivity over a broader range of conditions and across multiple years. Future studies could address this issue by measuring submesoscale motions and export properties (e.g., through thorium isotopes) through the late winter-early spring transition.

6. Conclusions

Data from the OSMOSIS project, using ocean gliders in the northeast Atlantic Ocean with biological and physical measurements, capture the full seasonal cycle of mixed layer and export variability at submesoscale resolution. In 2012–2013, a spring bloom occurs in May–June following a shoaling of the mixed layer; however, the timing of this bloom varies widely from year to year. Shorter restratification events occur as well throughout winter and may help to maintain phytoplankton populations. We consider the potential for subduction of water masses out of the surface ocean and associated export of fixed carbon from mixed layer, gravitational, and symmetric instabilities. MLI may be important, but accurately parameterizing its effects on subduction and export requires knowledge of the strength of the vertical stratification at the base of the mixed layer. Gravitational instabilities are important in determining the depth of the mixed layer but do not directly induce meaningful export. Symmetric instability is active in this region during winter and provides a clear mechanism for subduction of water masses from the surface; however, due to the highly episodic nature of this instability, it is difficult to assess its contribution to total export.

Although we found instances of subduction of water masses, we did not find evidence for substantial export of fixed carbon via this subductive route. Export through submesoscale instabilities requires both the production of unstable water columns and high fixed carbon concentrations at the surface. From this analysis, the influence from submesoscale motions at this location on export is small due to a limited overlap between strong vertical velocities across the base of the mixed layer associated with submesoscale instabilities, which are largest during winter, and fixed carbon concentrations in the surface of the ocean, which are largest in spring and summer. We point to the need for future work targeting this overlap window in other regions of the ocean.

Acknowledgments
We are grateful for the efforts of the entire OSMOSIS team and the crews of the RRS *Discovery*, the R/V *Celtic Explorer*, and the RRS *James Cook*. The authors thank Gillian Damerell, Stephanie Henson, Adrian Martin, Stuart Painter, and Nathan Briggs for helpful conversations related to this manuscript, as well as two anonymous reviewers for their comments. Glider data are held at the British Oceanographic Data Centre and are accessible at https://doi.org/10/cqc6. Code to generate the figures can be found at https://github.com/zerickso/GBC18. Satellite data were provided by NASA Goddard Space Flight Center at http://oceancolor.gsfc.nasa.gov. Meteorological data were supplied by ECMWF at http://apps.ecmwf.int/datasets/. Sea surface height was through AVISO data products at https://www.aviso.altimetry.fr/en/data.html. Color maps for Figures 1a, 5, 7, 8, and 10 are from the cmocean package by Kristen Thyng (https://matplotlib.org/cmocean/), and for Figure 12 the colormap is from the colorcet package by Peter Kovesi (https://github.com/bokeh/colorcet). The OSMOSIS project was funded by NERC grant NE/I019905/1 and NSFOCE-1155676, and the authors acknowledge funding from the David and Lucille Packard Foundation.

References

Alkire, M. B., D'Asaro, E., Lee, C., Perry, M. J., Gray, A., Cetinić, I., et al. (2012). Estimates of net community production and export using high-resolution, Lagrangian measurements of O_2, NO_3^-, and POC through the evolution of a spring diatom bloom in the North Atlantic. *Deep Sea Research Part I: Oceanographic Research Papers*, *64*, 157–174.

Armstrong, R. A., Lee, C., Hedges, J. I., Honjo, S., & Wakeham, S. G. (2002). A new, mechanistic model for organic carbon fluxes in the ocean based on the quantitative association of POC with ballast minerals. *Deep Sea Research Part II: Topical Studies in Oceanography*, *49*(1-3), 219–236.

Bachman, S., Fox-Kemper, B., Taylor, J., & Thomas, L. (2017). Parameterization of frontal symmetric instabilities. I: Theory for resolved fronts. *Ocean Modelling*, *109*, 72–95. https://doi.org/10.1016/j.ocemod.2016.12.003

Berelson, W. M. (2001). The flux of particulate organic carbon into the ocean interior: A comparison of four US JGOFS regional studies. *Oceanography*, *14*(4), 59–67.

Binetti, U. (2016). Dissolved oxygen-based annual biological production from glider observations at the Porcupine Abyssal Plain (North Atlantic) (PhD thesis), U. East Anglia.

Boccaletti, G., Ferrari, R., & Fox-Kemper, B. (2007). Mixed layer instabilities and restratification. *Journal of Physical Oceanography*, *37*(9), 2228–2250. https://doi.org/10.1175/JPO3101.1

Boss, E., Swift, D., Taylor, L., Brickley, P., Zaneveld, R., Riser, S., et al. (2008). Observations of pigment and particle distributions in the western North Atlantic from an autonomous float and ocean color satellite. *Limnology and Oceanography*, *53*, 2112–2122.

Brannigan, L. (2016). Intense submesoscale upwelling in anticyclonic eddies. *Geophysical Research Letters*, *43*, 3360–3369. https://doi.org/10.1002/2016GL067926

Brannigan, L., Marshall, D. P., Naveira-Garabato, A., & George Nurser, A. J. (2015). The seasonal cycle of submesoscale flows. *Ocean Modelling*, *92*, 69–84. https://doi.org/10.1016/j.ocemod.2015.05.002

Brannigan, L., Marshall, D. P., Naveira-Garabato, A. C., George Nurser, A., & Kaiser, J. (2017). *Submesoscale instabilities in mesoscale eddies* (Vol. 47, pp. 3085).

Briggs, N., Perry, M. J., Cetinić, I., Lee, C., D'Asaro, E., Gray, A. M., & Rehm, E. (2011). High-resolution observations of aggregate flux during a sub-polar North Atlantic spring bloom. *Deep Sea Research Part I: Oceanographic Research Papers*, *58*(10), 1031–1039. https://doi.org/10.1016/j.dsr.2011.07.007

Broecker, W. S., Peacock, S. L., Walker, S., Weiss, R., Fahrbach, E., Schroeder, M., et al. (1998). How much deep water is formed in the Southern Ocean?*Journal of Geophysical Research*, *103*(C8), 15,833–15,843. https://doi.org/10.1029/98JC00248

Buckingham, C. E., Naveira Garabato, A. C., Thompson, A. F., Brannigan, L., Lazar, A., Marshall, D. P., et al. (2016). Seasonality of submesoscale flows in the ocean surface boundary layer. *Geophysical Research Letters*, *43*, 2118–2126. https://doi.org/10.1002/2016GL068009

Callies, J., Ferrari, R., Klymak, J. M., & Gula, J. (2015). Seasonality in submesoscale turbulence. *Nature Communications*, *6*, 6862.

Callies, J., Flierl, G., Ferrari, R., & Fox-Kemper, B. (2016). The role of mixed-layer instabilities in submesoscale turbulence. *Journal of Fluid Mechanics*, *788*, 5–41.

Carlson, C. A., Ducklow, H. W., & Michaels, A. F. (1994). Annual flux of dissolved organic carbon from the euphotic zone in the northwestern Sargasso Sea. *Nature*, *371*(6496), 405.

Cetinić, I., Perry, M. J., D'Asaro, E., Briggs, N., Poulton, N., Sieracki, M. E., & Lee, C. M. (2015). A simple optical index shows spatial and temporal heterogeneity in phytoplankton community composition during the 2008 North Atlantic Bloom Experiment. *Biogeosciences*, *12*(7), 2179–2194. https://doi.org/10.5194/bg-12-2179-2015

Cullen, J. J., & Lewis, M. R. (1995). Biological processes and optical measurements near the sea surface: Some issues relevant to remote sensing. *Journal of Geophysical Research*, *100*(C7), 13,255–13,266. https://doi.org/10.1029/95JC00454

Daly, K. L., Bryne, R. H., Dickson, A. G., Gallager, S. M., Perry, M. J., & Tivey, M. K. (2004). Chemical and biological sensors for time-series research: Current status and new directions. *Marine Technology Society Journal*, *38*, 121–143.

Damerell, G. M., Heywood, K. J., Thompson, A. F., Binetti, U., & Kaiser, J. (2016). The vertical structure of upper ocean variability at the Porcupine Abyssal Plain during 2012–2013. *Journal Geophysical Research: Oceans*, *121*, 3075–3089. https://doi.org/10.1002/2015JC011423

Danabasoglu, G., Yeager, S. G., Bailey, D., Behrens, E., Bentsen, M., Bi, D., et al. (2014). North Atlantic simulations in Coordinated Ocean-Ice Reference Experiments Phase II (CORE-II). Part I: Mean states. *Ocean Modelling*, *73*, 76–107.

de Boyer Montégut, C., Madec, G., Fischer, A. S., Lazar, A., & Iudicone, D. (2004). Mixed layer depth over the global ocean: An examination of profile data and a profile-based climatology. *Journal of Geophysical Research*, *109*, C12003. https://doi.org/10.1029/2004JC002378

Dong, S., Sprintall, J., Gille, S. T., & Talley, L. (2008). Southern Ocean mixed-layer depth from Argo float profiles. *Journal of Geophysical Research*, *113*, C06013. https://doi.org/10.1029/2006JC004051

Ducklow, H. W., Steinberg, D. K., & Buesseler, K. O. (2001). Upper ocean carbon export and the biological pump. *Oceanography*, *14*(4), 50–58.

Erickson, Z. K., Thompson, A. F., Cassar, N., Sprintall, J., & Mazloff, M. R. (2016). An advective mechanism for deep chlorophyll maxima formation in southern Drake Passage. *Geophysical Research Letters*, *43*, 10,846–10,855. https://doi.org/10.1002/2016GL070565

Estapa, M. L., Siegel, D. A., Buesseler, K. O., Stanley, R. H., Lomas, M. W., & Nelson, N. (2015). Decoupling of net community and export production on submesoscales in the Sargasso Sea. *Global Biogeochemical Cycles*, *29*(8), 1266–1282.

Field, C. B., Behrenfeld, M. J., Randerson, J. T., & Falkowski, P. (1998). Primary production of the biosphere: Integrating terrestrial and oceanic components. *Science*, *281*(5374), 237–240. https://doi.org/10.1126/science.281.5374.237

Fox-Kemper, B., Danabasoglu, G., Ferrari, R., Griffies, S., Hallberg, R., Holland, M., et al. (2011). Parameterization of mixed layer eddies. III: Implementation and impact in global ocean climate simulations. *Ocean Modelling*, *39*(1-2), 61–78.

Fox-Kemper, B., Ferrari, R., & Hallberg, R. (2008). Parameterization of mixed layer eddies. Part I: Theory and diagnosis. *Journal of Physical Oceanography*, *38*(6), 1145–1165. https://doi.org/10.1175/2007JPO3792.1

Gent, P. R., Danabasoglu, G., Donner, L. J., Holland, M. M., Hunke, E. C., Jayne, S. R., et al. (2011). The Community Climate System Model version 4. *Journal of Climate*, *24*(19), 4973–4991.

Haine, T. W., & Marshall, J. (1998). Gravitational, symmetric, and baroclinic instability of the ocean mixed layer. *Journal of Physical Oceanography*, *28*(4), 634–658.

Hartman, S., Larkin, K., Lampitt, R., Lankhorst, M., & Hydes, D. (2010). Seasonal and inter-annual biogeochemical variations in the Porcupine Abyssal Plain 2003–2005 associated with winter mixing and surface circulation. *Deep-Sea Research Part II*, *57*(15), 1303–1312. https://doi.org/10.1016/j.dsr2.2010.01.007

Hemsley, V. S., Smyth, T. J., Martin, A. P., Frajka-Williams, E., Thompson, A. F., Damerell, G., & Painter, S. C. (2015). Estimating oceanic primary production using vertical irradiance and chlorophyll profiles from ocean gliders in the North Atlantic. *Environmental Science & Technology*, *49*(19), 11,612–11,621. https://doi.org/10.1021/acs.est.5b00608

Henson, S. A., & Thomas, A. C. (2008). A census of oceanic anticyclonic eddies in the Gulf of Alaska. *Deep Sea Research Part I: Oceanographic Research Papers*, *55*(2), 163–176.
Hood, R. R., Abbott, M. R., & Huyer, A. (1991). Phytoplankton and photosynthetic light response in the coastal transition zone off Northern California in June 1987. *Journal of Geophysical Research*, *96*(C8), 14,769–14,780. https://doi.org/10.1029/91JC01208
Hoskins, B. (1974). The role of potential vorticity in symmetric stability and instability. *Quarterly Journal of the Royal Meteorological Society*, *100*(425), 480–482.
Hurrell, J. W., Holland, M. M., Gent, P. R., Ghan, S., Kay, J. E., Kushner, P. J., et al. (2013). The Community Earth System Model: A framework for collaborative research. *Bulletin of the American Meteorological Society*, *94*(9), 1339–1360.
Jacox, M. G., Edwards, C. A., Kahru, M., Rudnick, D. L., & Kudela, R. M. (2015). The potential for improving remote primary productivity estimates through subsurface chlorophyll and irradiance measurement. *Deep Sea Research Part II: Topical Studies in Oceanography*, *112*(Supplement C), 107–116. https://doi.org/10.1016/j.dsr2.2013.12.008
Kostadinov, T. S., Siegel, D. A., & Maritorena, S. (2009). Retrieval of the particle size distribution from satellite ocean color observations. *Journal of Geophysical Research*, *114*(C9), C09015. https://doi.org/10.1029/2009JC005303
Lacour, L., Ardyna, M., Stec, K. F., Claustre, H., Prieur, L., Poteau, A., et al. (2017). Unexpected winter phytoplankton blooms in the North Atlantic subpolar gyre. *Nature Geoscience*, *10*, 836–839. https://doi.org/10.1038/ngeo3035
Lampitt, R., Salter, I., de Cuevas, B., Hartman, S., Larkin, K., & Pebody, C. (2010). Long-term variability of downward particle flux in the deep northeast Atlantic: Causes and trends. *Deep Sea Research Part II: Topical Studies in Oceanography*, *57*(15), 1346–1361. https://doi.org/10.1016/j.dsr2.2010.01.011
Laws, E. A., Falkowski, P. G., Smith, W. O., Ducklow, H., & McCarthy, J. J. (2000). Temperature effects on export production in the open ocean. *Global Biogeochemical Cycles*, *14*(4), 1231–1246. https://doi.org/10.1029/1999GB001229
Lévy, M., Ferrari, R., Franks, P. J., Martin, A. P., & Rivière, P. (2012). Bringing physics to life at the submesoscale. *Geophysical Research Letters*, *39*, L14602. https://doi.org/10.1029/2012GL052756
Lévy, M., Klein, P., & Treguier, A.-M. (2001). Impact of sub-mesoscale physics on production and subduction of phytoplankton in an oligotrophic regime. *Journal of Marine Research*, *59*(4), 535–565.
Mahadevan, A. (2016). The impact of submesoscale physics on primary productivity of plankton. *Annual Review of Marine Science*, *8*, 161–184.
Mahadevan, A., & Archer, D. (2000). Modeling the impact of fronts and mesoscale circulation on the nutrient supply and biogeochemistry of the upper ocean. *Journal of Geophysical Research*, *105*, 1209–1225. https://doi.org/10.1029/1999JC900216
Mahadevan, A., D'Asaro, E., Lee, C., & Perry, M. J. (2012). Eddy-driven stratification initiates North Atlantic spring phytoplankton blooms. *Science*, *337*(6090), 54–58. https://doi.org/10.1126/science.1218740
Mahadevan, A., & Tandon, A. (2006). An analysis of mechanisms for submesoscale vertical motion at ocean fronts. *Ocean Modelling*, *14*, 241–256. https://doi.org/10.1016/j.ocemod.2006.05.006
Martin, A. P., Lucas, M. I., Painter, S. C., Pidcock, R., Prandke, H., Prandke, H., & Stinchcombe, M. C. (2010). The supply of nutrients due to vertical turbulent mixing: A study at the Porcupine Abyssal Plain study site in the northeast Atlantic. *Deep Sea Research Part II: Topical Studies in Oceanography*, *57*(15), 1293–1302. https://doi.org/10.1016/j.dsr2.2010.01.006
McWilliams, J. C. (2016). Submesoscale currents in the ocean. In *Proc. R. Soc. A* (Vol. 472, p. 20160117). The Royal Society.
Molemaker, M. J., McWilliams, J. C., & Dewar, W. K. (2015). Submesoscale instability and generation of mesoscale anticyclones near a separation of the California undercurrent. *Journal of Physical Oceanography*, *45*(3), 613–629. https://doi.org/10.1175/JPO-D-13-0225.1
Neori, A., Holm-Hansen, O., Mitchell, B. G., & Kiefer, D. A. (1984). Photoadaptation in marine phytoplankton. *Plant Physiology*, *76*(2), 518–524.
Omand, M. M., D'Asaro, E. A., Lee, C. M., Perry, M. J., Briggs, N., Cetinić, I., & Mahadevan, A. (2015). Eddy-driven subduction exports particulate organic carbon from the spring bloom. *Science*, *348*, 222–225.
Painter, S. C., Lucas, M. I., Stinchcombe, M. C., Bibby, T. S., & Poulton, A. J. (2010). Summertime trends in pelagic biogeochemistry at the Porcupine Abyssal Plain study site in the northeast Atlantic. *Deep Sea Research Part II: Topical Studies in Oceanography*, *57*(15), 1313–1323.
Rocha, C. B., Chereskin, T. K., Gille, S. T., & Menemenlis, D. (2016). Mesoscale to submesoscale wavenumber spectra in Drake Passage. *Journal of Physical Oceanography*, *46*, 601–620. https://doi.org/10.1175/JPO-D-15-0087.1
Rocha, C. B., Gille, S. T., Chereskin, T. K., & Menemenlis, D. (2016). Seasonality of submesoscale dynamics in the Kuroshio Extension. *Geophysical Research Letters*, *43*, 11,304–11,311. https://doi.org/10.1002/2016GL071349
Roesler, C., Uitz, J., Claustre, H., Boss, E., Xing, X., Organelli, E., et al. (2017). Recommendations for obtaining unbiased chlorophyll estimates from in situ chlorophyll fluorometers: A global analysis of WET Labs ECO sensors. *Limnology and Oceanography: Methods*, *15*(6), 572–585. https://doi.org/10.1002/lom3.10185
Rosso, I., Hogg, A. M., Strutton, P. G., Kiss, A. E., Matear, R., Klocker, A., & van Sebille, E. (2014). Vertical transport in the ocean due to sub-mesoscale structures: Impacts in the Kerguelen region. *Ocean Modelling*, *80*, 10–23. https://doi.org/10.1016/j.ocemod.2014.05.001
Rudnick, D. L. (2001). On the skewness of vorticity in the upper ocean. *Geophysical Research Letters*, *28*(10), 2045–2048.
Rumyantseva, A., Lucas, N., Rippeth, T., Martin, A., Painter, S. C., Boyd, T. J., & Henson, S. (2015). Ocean nutrient pathways associated with the passage of a storm. *Global Biogeochemical Cycles*, *29*(8), 1179–1189. https://doi.org/10.1002/2015GB005097
Sarmiento, J. (1983). A tritium box model of the North Atlantic thermocline. *Journal of Physical Oceanography*, *13*(7), 1269–1274.
Sarmiento, J. L., Thiele, G., Key, R. M., & Moore, W. S. (1990). Oxygen and nitrate new production and remineralization in the North Atlantic subtropical gyre. *Journal of Geophysical Research*, *95*(C10), 18,303–18,315.
Sasaki, H., Klein, P., Qiu, B., & Sasai, Y. (2014). Impact of oceanic-scale interactions on the seasonal modulation of ocean dynamics by the atmosphere. *Nature Communications*, *5*, 5636. https://doi.org/10.1038/ncomms6636
Stemmann, L., Jackson, G. A., & Ianson, D. (2004). A vertical model of particle size distributions and fluxes in the midwater column that includes biological and physical processes? Part I: Model formulation. *Deep Sea Research Part I: Oceanographic Research Papers*, *51*(7), 865–884.
Stukel, M. R., Aluwihare, L. I., Barbeau, K. A., Chekalyuk, A. M., Goericke, R., Miller, A. J., et al. (2017). Mesoscale ocean fronts enhance carbon export due to gravitational sinking and subduction. *Proceedings of the National Academy of Sciences*, *114*(6), 1252–1257.
Su, Z., Wang, J., Klein, P., Thompson, A. F., & Menemenlis, D. (2018). Ocean submesoscales as a key component of the global heat budget. *Nature Communications*, *9*(1), 775.
Sverdrup, H. U. (1953). On conditions for the vernal blooming of phytoplankton. *ICES Journal of Marine Science*, *18*(3), 287–295. https://doi.org/10.1093/icesjms/18.3.287
Taylor, J. R., & Ferrari, R. (2009). On the equilibration of a symmetrically unstable front via a secondary shear instability. *Journal of Fluid Mechanics*, *622*, 103–113. https://doi.org/10.1017/S0022112008005272
Taylor, J. R., & Ferrari, R. (2010). Buoyancy and wind-driven convection at mixed layer density fronts. *Journal of Physical Oceanography*, *40*(6), 1222–1242.

Thomas, L. N., & Lee, C. M. (2005). Intensification of ocean fronts by down-front winds. *Journal of Physical Oceanography*, *35*(6), 1086–1102.
Thomas, L. N., Taylor, J. R., D'Asaro, E. A., Lee, C. M., Klymak, J. M., & Shcherbina, A. (2016). Symmetric instability, inertial oscillations, and turbulence at the Gulf Stream front. *Journal of Physical Oceanography*, *46*(1), 197–217.
Thomas, L. N., Taylor, J. R., Ferrari, R., & Joyce, T. M. (2013). Symmetric instability in the Gulf Stream. *Deep-Sea Research Part II*, *91*, 96–110.
Thompson, A. F., Lazar, A., Buckingham, C., Naveira Garabato, A. C., Damerell, G. M., & Heywood, K. J. (2016). Open-ocean submesoscale motions: A full seasonal cycle of mixed layer instabilities from gliders. *Journal of Physical Oceanography*, *46*(4), 1285–1307.
Tjiputra, J., Roelandt, C., Bentsen, M., Lawrence, D., Lorentzen, T., Schwinger, J., et al. (2013). Evaluation of the carbon cycle components in the Norwegian Earth System Model (NorESM). *Geoscientific Model Development*, *6*(2), 301–325.
Washburn, L., Kadko, D. C., Jones, B. H., Hayward, T., Kosro, P. M., Stanton, T. P., et al. (1991). Water mass subduction and the transport of phytoplankton in a coastal upwelling system. *Journal of Geophysical Research*, *96*(C8), 14,927–14,945. https://doi.org/10.1029/91JC01145
Whitt, D., Taylor, J. R., & Lévy, M. (2017). Synoptic-to-planetary scale wind variability enhances phytoplankton biomass at ocean fronts. *Journal of Geophysical Research: Oceans*, *122*, 4602–4633. https://doi.org/10.1002/2016JC011899
Xing, X., Morel, A., Claustre, H., Antoine, D., D'Ortenzio, F., Poteau, A., & Mignot, A. (2011). Combined processing and mutual interpretation of radiometry and fluorimetry from autonomous profiling bio-argo floats: Chlorophyll a retrieval. *Journal of Geophysical Research*, *116*, C06020. https://doi.org/10.1029/2010JC006899

Erratum

In the originally published version of this paper, Figure 5, panel (a) was incorrect. The figure has since been corrected, and this version may be considered the authoritative version of record.